Reflection Reduction Through Modal Filtering for Integrated Antenna Measurements Above 100 GHz

Linus Boehm, *Student Member, IEEE*, Alexander Foerstner, Martin Hitzler, *Student Member, IEEE*, and Christian Waldschmidt, *Senior Member, IEEE*

***Abstract*— Feeding integrated antennas during a measurement requires special feeding structures. Due to the small antenna dimensions, these feeding structures are often much bigger than the antenna under test (AUT) itself and with chip sizes of around 1 mm^2, the achievable separation between antenna and feed is limited. Wafer probes have to be used to feed the AUT during passive antenna measurements and present a large reflective surface in close proximity to the AUT. Reflections from the wafer probe cause interference on the measurement surface and distort the results. The same is true for active antenna measurements, where bondwires and the package can have a significant effect on the radiated fields. The fragility and size of the components do not allow to reduce reflections with absorbers, which is why modal filtering was used in this paper to mitigate undesired reflections and improve the measurement result through postprocessing. Two issues that limit the performance of the algorithm are discussed, namely, phase center inaccuracies of the AUT and a limited measurement surface. It is shown that modal filtering is applicable to integrated antenna measurements at frequencies over 100 GHz and that a significant improvement in the measured radiation pattern can be achieved. Furthermore, it is shown that the postprocessed results make it possible to measure the directivity of integrated antennas, despite strong probe reflections.**

***Index Terms*— Antenna measurement, integrated antenna, mathematical absorber reflection suppression (MARS), millimeter-wave, modal filtering, phase center, spherical wave expansion (SWE), wafer probe.**

I. Introduction

IDEALLY, antennas should be measured in free space with no objects in the measurement environment to interfere with the radiated fields; however, this is not possible in a real setup. The required measurementequipment, feeding structures, and mechanical setup can often not be sufficiently shielded to achieve the desired accuracy. Therefore, other measures have to be implemented to reduce unwanted influences of the measurement environment on the results.

One possibility is postprocessing the data to separate the desired radiation from unwanted reflections in order to suppress interferences. A common approach to separate different paths of propagation in time domain is by Fourier transforming a broadband measurement [1]. However, time gating requires large bandwidths of the measurement setup and antennas under test (AUTs) for a sufficient temporal resolution, especially for reflections that occur close to the AUT.

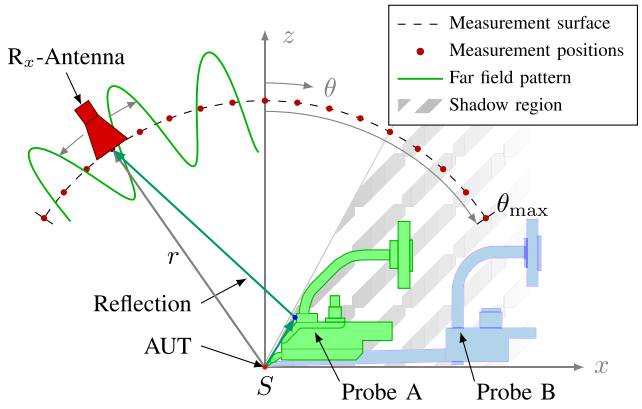

Fig. 1. Wafer probe reflections cause interference on the measurement surface. Signal blockage in the shadow region behind the probe. Measurement surface is limited by $\theta_{\max}$.

A different method is the mathematical absorber reflection suppression (MARS) algorithm, which was presented in [2] for a spherical near-field range and is based on modal filtering. The measured fields are being represented with orthogonal basis functions or modes to achieve a modal separation between the desired and reflected signals. It can be applied to various measurement surfaces depending on the used basis functions, e.g., spherical [3], cylindrical [4]–[6], and planar [7] near-field measurements as well as far-field [8], [9] measurements.

The algorithm was used for an antenna fed with a wafer probe in [10], using the 60-GHz patch antenna presented in [11] as AUT. For integrated antennas at frequencies over 100 GHz, wafer probes are the only applicable option to feed antennas that are not fed directly from active on-chip circuitry. Due to the comparatively large size and the proximity to the AUT, wafer probes distort antenna measurements significantly [12], as shown in Fig. 1. Custom made wafer probes (probe B in Fig. 1) can be used to reduce the interference [13], [14], but they are expensive and difficult to fabricate. The fragility of wafer probes and the small distance to the AUT do not allow for covering the probes with absorbers,

Manuscript received January 13, 2017; revised April 19, 2017; accepted May 9, 2017. Date of publication May 17, 2017; date of current version July 1, 2017. This work was supported by the German Research Foundation under Project WA 3506/1-1. *(Corresponding author: Linus Boehm.)*

The authors are with Ulm University, 89081 Ulm, Germany (e-mail: linus.boehm@uni-ulm.de).

Color versions of one or more of the figures in this paper are available online at http://ieeexplore.ieee.org.

Digital Object Identifier 10.1109/TAP.2017.2705225

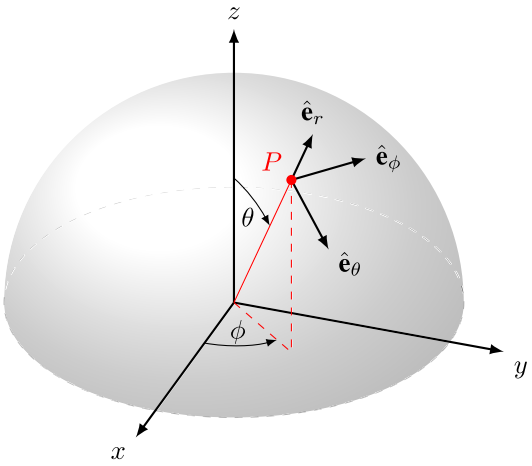

Fig. 2. Definition of the spherical coordinates ($0 \le \phi < 2\pi$, $0 \le \theta \le \pi$).

which is why postprocessing is used in this paper to obtain meaningful measurement results, despite the strong reflections from standard probes (probe A in Fig. 1).

The AUT that was used for all simulations and measurements was a scaled version of [15], designed for 160 GHz.

Section II describes the spherical wave expansion (SWE), required for the MARS algorithm explained in Section III. The impact of a limited scanning surface (see Fig. 1) and an inaccurate phase center location on the calculated coefficients is discussed in Sections IV and V, respectively. Section V also introduces a new method to determine the phase center of an AUT from disturbed measurement data. Section VI shows the results of the MARS algorithm applied to an integrated antenna measurement at 160 GHz for radiation pattern and directivity, and demonstrates that the influence of reflections can be reduced significantly.

II. Modal Filtering

Modal filtering can be implemented for different scanning surfaces, such as planar, cylindrical, and spherical measurement geometries. The small dimensions of integrated antennas allow to perform far-field measurements at relatively small distances, which is why the far-field approach with a spherical scanning geometry is used in this paper. In the case of a current-free and lossless space, the scalar wave equation is

$$\Delta\psi(\mathbf{r}) + k^2\psi(\mathbf{r}) = 0 \tag{1}$$

where $k = 2\pi/\lambda$ is the wavenumber. In this paper, only the r-component of $\boldsymbol{\psi}(\mathbf{r})$ is considered. Assuming that the solution can be written as a product of functions that only depend on a single coordinate, separation of variables can be used. For a spherical coordinate system, as shown in Fig. 2, the ansatz is [16]

$$\psi(r,\theta,\phi) = R(r)\Theta(\theta)\Phi(\phi). \tag{2}$$

A solution to the wave equation can now be calculated as shown in [17] and has the form of

$$\psi_{mn}^{(i)}(\mathbf{r}) = z_n^{(i)}(kr)\bar{P}_n^{|m|}(\cos\theta)e^{jm\phi}. \tag{3}$$

The ϕ dependence is specified through a complex exponential function, while the variation in θ-direction is expressed through the normalized associated Legendre function of the degree n and order m

$$\bar{P}_n^m(x) = \sqrt{\frac{2n+1}{2}\frac{(n-m)!}{(n+m)!}}P_n^m(x) \tag{4}$$

with

$$P_n^m(x) = \frac{(1-x^2)^{m/2}}{2^n n!}\frac{d^{n+m}}{dx^{n+m}}(x^2-1)^n. \tag{5}$$

The limits of the modal indices m and n in $\psi_{mn}^{(i)}(r)$ are $0 \le n \le \infty$ and $-n \le m \le n$, respectively.

Four different solutions in the r-direction can be given, which apply to different modes of propagation. Bessel or Neumann functions $z_n^{(1,2)}(kr)$ can be chosen for standing waves, the spherical Hankel function of the first kind $z_n^{(3)}(kr)$ represents propagation in negative r-direction, but in the case of propagation in positive r-direction, the spherical Hankel function of the second kind is the most suitable solution, and therefore, $z_n^{(i)}(kr)$ is set to

$$z_n^{(4)}(kr) = h_n^{(2)}(kr). \tag{6}$$

In this paper, the following far-field approximation was used:

$$h_n^{(2)}(kr) \overset{kr\to\infty}{\approx} j^{n+1}\frac{e^{-jkr}}{kr}. \tag{7}$$

The radiated electrical field can be split in a transverse electric (TE) and a transverse magnetic (TM) component [8]

$$\mathbf{E} = \underbrace{\nabla\times r\hat{\mathbf{e}}_r\psi_{mn}^{(4)}(\mathbf{r})}_{=\mathbf{m}_{mn}^{(4)}(\mathrm{TE})} + \underbrace{\frac{1}{k}\nabla\times\left(\nabla\times r\hat{\mathbf{e}}_r\psi_{mn}^{(4)}(\mathbf{r})\right)}_{=\mathbf{n}_{mn}^{(4)}(\mathrm{TM})}. \tag{8}$$

$\mathbf{m}_{mn}^{(4)}$ and $\mathbf{n}_{mn}^{(4)}$ are spherical wave functions that can be normalized to [18]

$$\begin{aligned}\mathbf{M}_{mn}^{(4)}(\mathbf{r}) &= A\cdot\mathbf{m}_{mn}^{(4)}(\mathbf{r})\\ \mathbf{N}_{mn}^{(4)}(\mathbf{r}) &= A\cdot\mathbf{n}_{mn}^{(4)}(\mathbf{r})\end{aligned} \tag{9}$$

with

$$A = \frac{1}{\sqrt{2\pi n(n+1)}}\cdot\begin{cases}1, & \text{if } m=0\\ \left(-\dfrac{m}{|m|}\right)^m, & \text{otherwise.}\end{cases} \tag{10}$$

The radiated electric field can now be written as a weighted sum of the power normalized spherical wave functions $\mathbf{M}_{mn}^{(4)}(\mathbf{r})$ and $\mathbf{N}_{mn}^{(4)}(\mathbf{r})$

$$\mathbf{E}(\mathbf{r}) = \frac{k}{\sqrt{\eta}}\sum_{n=1}^{\infty}\sum_{m=-n}^{n}\left[B_{mn}^{(1)}\mathbf{M}_{mn}^{(4)}(\mathbf{r}) + B_{mn}^{(2)}\mathbf{N}_{mn}^{(4)}(\mathbf{r})\right]. \tag{11}$$

The complex weighting factors $B_{mn}^{(1)}$ and $B_{mn}^{(2)}$ are called spherical mode coefficients (SMCs) [8]. The factor $k/\sqrt{\eta}$, with $\eta = \sqrt{\varepsilon/\mu}$, ensures that $B_{mn}^{(1)}$ and $B_{mn}^{(2)}$ have the unit $W^{1/2}$. Together with (4) and (9), this allows to calculate the total radiated power as a simple summation over the SMCs

$$P = \frac{1}{2}\sum_{n=1}^{\infty}\sum_{m=-n}^{n}\left[\left|B_{mn}^{(1)}\right|^2 + \left|B_{mn}^{(2)}\right|^2\right]. \tag{12}$$

After the calculation of $\mathbf{m}_{mn}^{(4)}$ and $\mathbf{n}_{mn}^{(4)}$ with (8) and splitting $\mathbf{E}(\mathbf{r})$ in an E_ϕ and E_θ component, (11) can be solved for $B_{mn}^{(1)}$ and $B_{mn}^{(2)}$ as shown in [18]. The SMCs can then be calculated with

$$B_{mn}^{(1)} = \frac{\sqrt{\eta}(-1)^m}{k h_n^{(2)}(kr_1)} \frac{1}{\sqrt{2\pi n(n+1)}} \left(-\frac{m}{|m|}\right)^m \cdot \int_{\phi=0}^{2\pi} \int_{\theta=0}^{\pi} \left[E_\theta(\mathbf{r}_1) \left(-\frac{jm}{\sin\theta} \bar{P}_n^{|m|}(\cos\theta) \right) + E_\phi(\mathbf{r}_1) \left(-\frac{\partial \bar{P}_n^{|m|}(\cos\theta)}{\partial\theta} \right) \right] \times e^{-jm\phi} \sin\theta d\theta d \quad (13)$$

and

$$B_{mn}^{(2)} = \frac{\sqrt{\eta}(-1)^m}{k \left[\frac{1}{kr_1} \frac{\partial\, (kr_1 h_n^{(2)}(kr_1))}{\partial kr_1} \right]} \frac{1}{\sqrt{2\pi n(n+1)}} \left(-\frac{m}{|m|}\right)^m \cdot \int_{\phi=0}^{2\pi} \int_{\theta=0}^{\pi} \left[E_\theta(\mathbf{r}_1) \left(\frac{\partial \bar{P}_n^{|m|}(\cos\theta)}{\partial\theta} \right) + E_\phi(\mathbf{r}_1) \left(-\frac{jm}{\sin\theta} \bar{P}_n^{|m|}(\cos\theta) \right) \right] \times e^{-jm\phi} \sin\theta d\theta d\phi \quad (14)$$

where r_1 is the measurement distance and $\mathbf{r}_1 = (r_1, \phi, \theta)$ is a point on the measurement surface. Equation (11) shows that an infinite number of spherical wave functions have to be added in order to calculate the radiated field. However, the function values of the Hankel function $h_n^{(2)}(kr)$ decline strongly for $n > kr_0$ [see (7)], where r_0 is the minimum radius of a sphere around the center of the coordinate system that envelops the aperture of the source [minimum radius sphere (MRS)]. This means that modes with a degree $n > kr_0$ are attenuated significantly compared with lower degree modes and can be neglected for the far-field calculation. Thus, the summation in (11) can be confined to SMCs of degree $1 \leq n \leq N$ [18], with

$$N = \lfloor kr_0 \rfloor + n_1. \quad (15)$$

n_1 is a safety margin that ensures that no significant modes are truncated and $\lfloor x \rfloor$ denotes the floor function.

III. MARS

MARS is a combination of postprocessing and measurement technique that allows to reduce reflections that occurred during the measurement and uses SWE to separate direct radiation from reflections.

As shown in (15), the number of modes required to represent the radiated fields of an antenna depends on the AUT size, which means that an antenna with an MRS of r_0 is fully described by SMCs of degree $n \leq N$. Modes of a higher degree can, therefore, be attributed to interferences, which can then be suppressed by using only lower degree modes

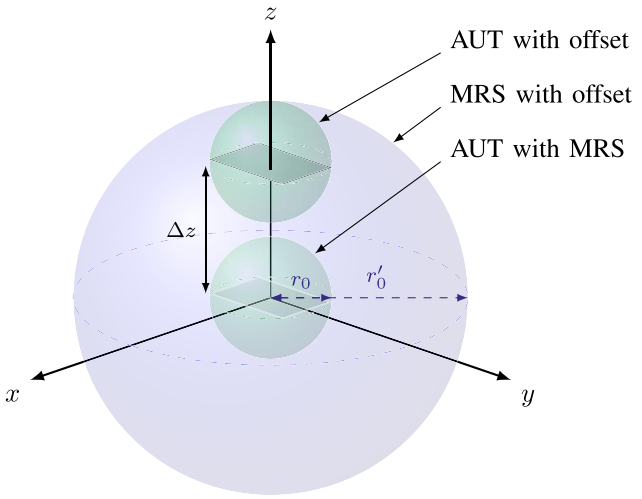

Fig. 3. AUT offset increases the size of the MRS and the amount of modes required for the far-field representation.

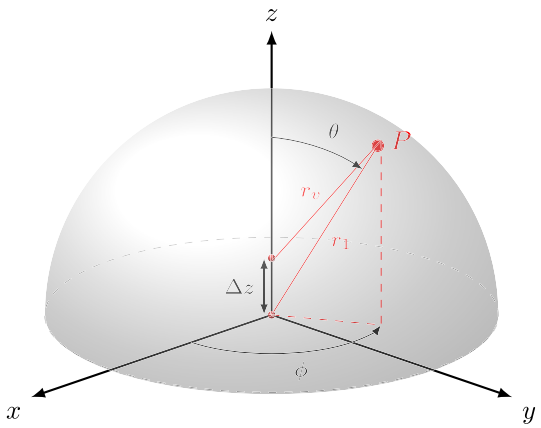

Fig. 4. Path difference between the original measurement distance r and the distance r_v of the updated position for an offset of Δz.

for the back transformation into the far field. The remaining coefficients are

$$B_{mn}^{(s)}(n > N) = 0, \quad s = 1, 2. \quad (16)$$

Therefore, the further antenna and reflection mode coefficients are apart, the better reflections can be canceled out.

For MARS, the measurement is performed with an out-of-center AUT, with an offset of $\Delta z > 2r_0$. This offset position increases the size of the MRS as shown in Fig. 3. As the measurement is not performed around the phase center, the phase change of the field on the measurement surface is increased as well. Thus, the SMCs are spread over a larger region in the mode spectrum. The AUT can then be moved back to the origin of the measurement surface by adjusting the phase and amplitude of the measured values to account for the path difference $\Delta r(\theta, \phi) = |\mathbf{r}_1(\theta, \phi)| - |\mathbf{r}_v(\theta, \phi)|$ between the real measurement distance $|\mathbf{r}_v(\theta, \phi)| = r_v(\theta, \phi)$ and the desired measurement distance $|\mathbf{r}_1(\theta, \phi)| = r_1$, as shown in Fig. 4. This undoes the phase change caused by the offset position for direct radiation, focusing the AUT at lower degree modes, while further spreading reflections over the mode spectrum. Therefore, MARS increases the separation between wanted

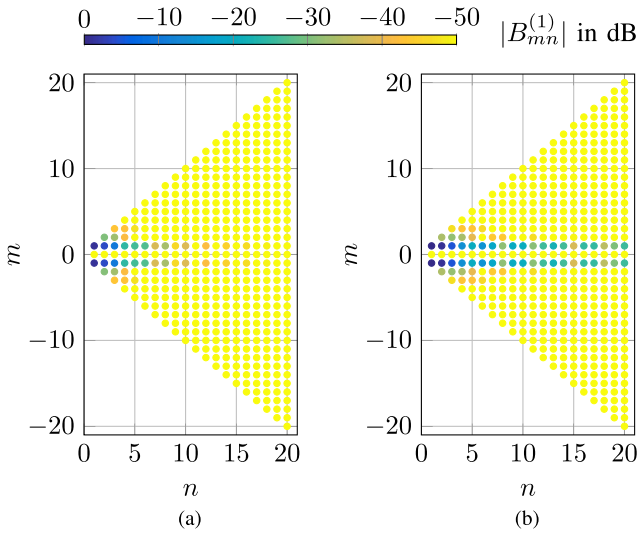

Fig. 5. Mode spectrum $B_{mn}^{(1)}$ of the simulated AUT at 160 GHz for different maximum scanning angles $\theta_{\max}$. (a) $\theta_{\max} = 90°$. (b) $\theta_{\max} = 50°$.

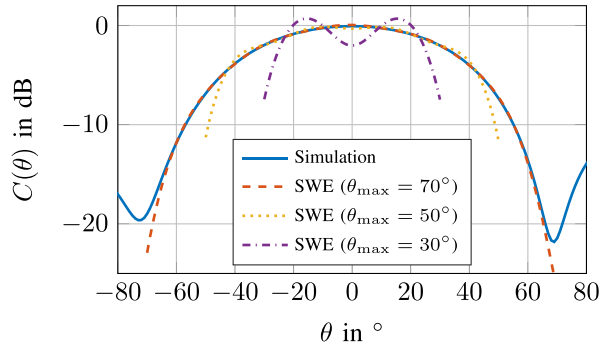

Fig. 6. Impact of a limited scanning surface on the calculated far field based on spherical wave coefficients of degree $N \leq 13$, E-plane.

and unwanted modes and improves the filter performance of the SWE.

The translated field can be calculated with

$$\mathbf{E}(\theta,\phi) = \left(\frac{r_v(\theta,\phi)}{r_1}\right)^2 \mathbf{E}_v(\theta,\phi) e^{-jk\Delta r(\theta,\phi)}. \quad (17)$$

IV. Limited Scanning Surface

Due to limitations of the measurement setups and the required feeding fixtures for the AUT, the radiated fields cannot be measured on a complete hemisphere around the AUT, which means that part of the field is truncated for postprocessing.

Fig. 5 shows the SMCs that were calculated based on a far-field pattern simulation of the integrated antenna. The triangular shape is due to the limits of m and n (see Section II). With $kr_0 = 3.3$, three spherical wave functions are sufficient to fully represent the field of the antenna, which is why the SMCs with $n \leq 3$ have much higher values than higher degree modes in Fig. 5(a). Fig. 5(b) shows the calculated SMCs of the same antenna, but based on far-field data with $\theta_{\max} = 50°$. The nonphysical truncation of the field leads to an increase of higher degree SMC values. Fig. 6 displays the calculated far field for different $\theta_{\max}$ values based on the coefficients with $n < 13$. The error between the original and the calculated far field increases for smaller scanning surfaces and the largest error occurs at the edge of the scanning surface.

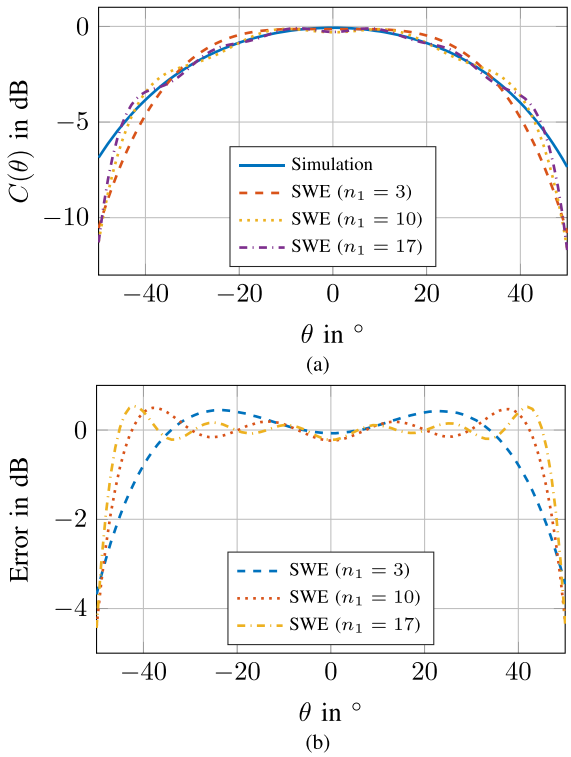

Fig. 7. Comparison of the calculated far-field pattern in the E-plane for different amounts of considered modes $N = 3 + n_1$ ($\theta_{\max} = 50°$). (a) Radiation pattern comparison. (b) Difference between simulation and calculation.

The impact of the safety margin n_1 is shown in Fig. 7, where the calculated far field and the deviation to the original field is displayed for $\theta_{\max} = 50°$. Fig. 7(b) shows that the difference between the simulated and the calculated far-field pattern decreases when more SMCs are considered, which means that the error can be reduced with a large safety margin. On the other hand, the number of SMCs has to be limited for the back transformation in order to mitigate reflections. $n_1 = 10$ proved to be a good compromise between filter performance and transformation accuracy and is used hereafter. The required computing time is around 10 s.

As the error shown in Fig. 7(b) is deterministic for a given radiation pattern, the error can be determined based on a simulation of the AUT and subtracted from the obtained far-field MARS result to further reduce the effect of a limited scanning surface (see Section VI). The error was calculated as $|C_{\text{sim}} - C_{\text{calc}}(n_1)|$.

A second option to mitigate the effect of a limited scanning surface would be to substitute missing measurement points with simulation data. However, this requires high phase agreement between simulation and measurement, which is difficult to achieve as the measurement environment with all scatterers has to be reproduced with very high accuracy in the simulation.

V. AUT Phase Center

In order to get the best separation between reflection modes and AUT modes, the measured far field has to be translated

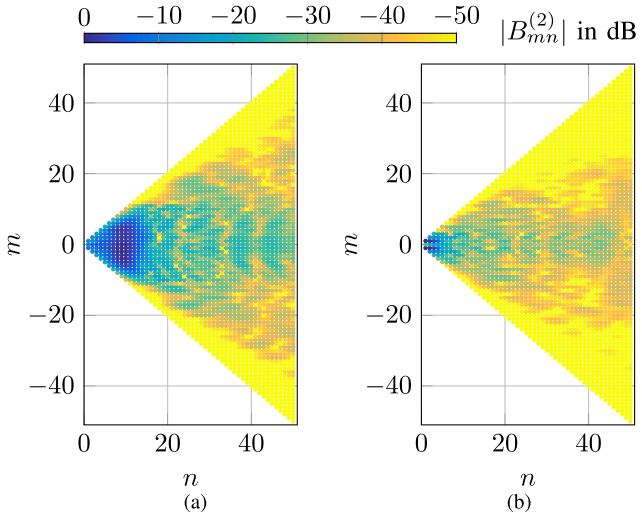

Fig. 8. $B_{mn}^{(2)}$ mode spectrum of the measurement (probe A) before and after translation of the far field into the calculated phase center, which focuses the coefficients at a few modes of low degree. (a) Measurement with offset. (b) Translated into phase center.

back to the phase center of the AUT, which concentrates the AUT at SMCs of low degree. Therefore, the position of the phase center has to be precisely known. With a wavelength of less than 2 mm and AUT dimensions of around 1 mm, the measurement of the phase center position is challenging.

Fig. 8(a) shows the calculated mode coefficients of the integrated antenna based on a measurement performed at 160 GHz. The AUT position was measured with a laser range finder and the measurement was performed around the expected AUT position with an offset of $\Delta z = 0$. The calculated coefficients do not show the desired concentration of the SMCs at modes of low degree, which indicates that the accuracy of the phase center position was not sufficient.

In order to obtain a more accurate phase center position, the phase center of the AUT can be calculated based on an initial radiation pattern measurement as shown in [19] and [20]. However, this so-called flip-test was only used for offsets and tilts in one plane and requires multiple measurements.

In this paper, two phase center calculation methods are used and compared. In the first method, the phase center is calculated based on a far field measurement at the distance r. If a far-field measurement is performed around the phase center of an antenna, the phase should ideally be constant on a spherical measurement surface. Thus, the phase center can be determined by optimizing the center of the measurement $\mathbf{c}$ in postprocessing, such that the phase change on the measurement surface is minimized.

The distance between the measurement positions $\mathbf{p}_i$ and the updated measurement center position $\mathbf{c}'$ is calculated with

$$r_i' = |\mathbf{p}_i - \mathbf{c}'|. \tag{18}$$

The difference between r and the new measurement distances r_i' is

$$\Delta r_i = r - r_i' \tag{19}$$

which corresponds to a phase change of $\Delta\phi_i = k\Delta r_i$. Therefore, the updated phase at each position is

$$S_{21,i}' = S_{21,i} e^{-j\Delta\phi_i}. \tag{20}$$

The phase center can now be found by minimizing the standard deviation of $\arg(S_{21,i}')$ for two orthogonal cuts of the measured far-field pattern.

However, strong reflections can alter the phase on the measurement surface, potentially leading to a false phase center position. This uncertainty of the phase center position impacts the postprocessing and causes errors in the calculated far-field pattern.

A new method to increase the accuracy of the phase center determination based on the calculated SMCs was implemented. As previously mentioned, the translation of the far field in the phase center focuses the SMCs in a small number of modes. If the AUT is translated into the correct phase center, the MRS has the smallest possible radius (see Fig. 3) and the number of relevant modes to represent the far field is minimal. Therefore, the amount of modes with significant magnitude can be used as a quality function for an optimization of the phase center position. In this case, the phase center position was chosen such that the number of SMCs with a magnitude larger than -5 dB was minimized. The Nelder–Mead method [21] was used and required around 70 iterations. The starting value was obtained from an initial far-field phase center calculation.

In order to compare the performance of the far field and the SWE approach for the phase center determination, an AUT was measured twice in the exact same position with two different wafer probes, A and B (see Fig. 1), that cause different interferences. Table I shows the calculated phase center offsets in x-, y-, and z-direction for both methods and probes. In the x- and y-plane, the calculated offsets for the far-field method deviate by around 300 μm between the two probe measurements, while the calculated offset values are almost identical when using the mode method. This clearly shows that the mode method is more robust toward interferences in the measurement setup and better suited to determine the phase center compared with the far-field method. However, the mode method is more likely to run in a local minimum in the case of a poor start value, which is why the initial guess was calculated with the far-field method.

The phase center position of a real antenna is not concentrated in one single point and changes with the frequency, θ, and ϕ [22], with the highest standard deviation in the direction of radiation, which is why the biggest deviations in Table I occur for δz.

Fig. 8(b) shows the calculated SMCs after the far field has been mathematically translated to the calculated phase center. Compared with Fig. 8(a), it shows that the coefficients are much more focused at modes of lower degree and order, which indicates that the calculated phase center position is accurate. The magnitude of the SMCs decreases significantly for degrees $n > 3$, which agrees with the expected result for the given antenna dimension and the simulation shown in Fig. 5(b). Comparatively high values of SMCs for degrees larger than ten are caused by the previously

TABLE I
CALCULATED OFFSET FROM THE PHASE CENTER OF THE AUT

Wafer probe	δx in mm A	δx in mm B	δy in mm A	δy in mm B	δz in mm A	δz in mm B
Far field method						
$\Delta z = 0$ mm	2.7	3.0	0.5	0.2	2.6	1.6
$\Delta z = 6$ mm	2.6	2.9	0.5	0.3	8.7	7.6
Mode method						
$\Delta z = 0$ mm	3.1	3.1	0.3	0.3	2.2	2.3
$\Delta z = 6$ mm	3.0	3.0	0.2	0.3	7.8	8.3

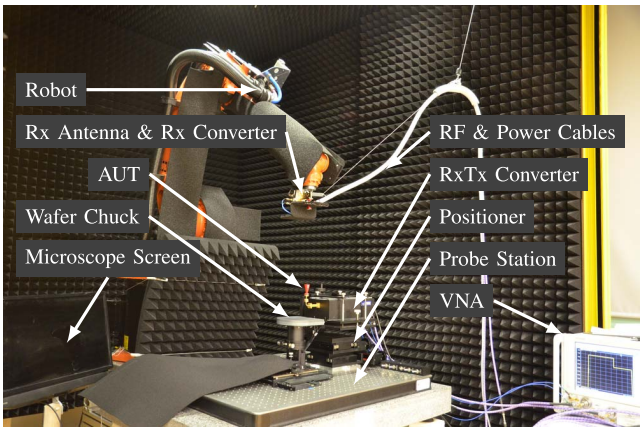

Fig. 9. Measurement setup with components.

mentioned strong reflections from the surface of the wafer probe [13].

VI. INTEGRATED ANTENNA MEASUREMENTS

Fig. 9 shows the robotic measurement setup that was used to perform the measurements. A detailed description of the setup can be found in [23].

Interference from wafer probes can disturb integrated antenna measurements such that the results are unfit for a meaningful AUT characterization and are the main source of reflection for integrated antenna measurements [13], [24]. Therefore, the MARS algorithm was applied to a wafer probe measurement to improve the result. Fig. 10 shows the calculated SMCs after translation into the calculated phase center of the AUT, focusing the SMCs at low-degree modes. As expected from the simulation shown in Fig. 5(b), Fig. 10(a) shows the same periodic mode pattern for coefficients with the order $m = \pm 1$, caused by the limited scanning surface around the AUT. The measurement was performed at a distance of 300 mm for a maximum angle $\theta_{\max} = 50°$ with an offset of $\Delta z = 6$ mm using a standard wafer probe (probe A). Most reflections occur within a distance of less than 20 mm of the AUT. This corresponds to modes with a degree of approximately 65, which is why higher degree modes are of negligible magnitude.

A. Radiation Pattern

Based on the SMCs of degree $n < 13$, the far field of the integrated antenna was calculated to obtain the radiation pattern without probe reflections. Fig. 11 shows a comparison

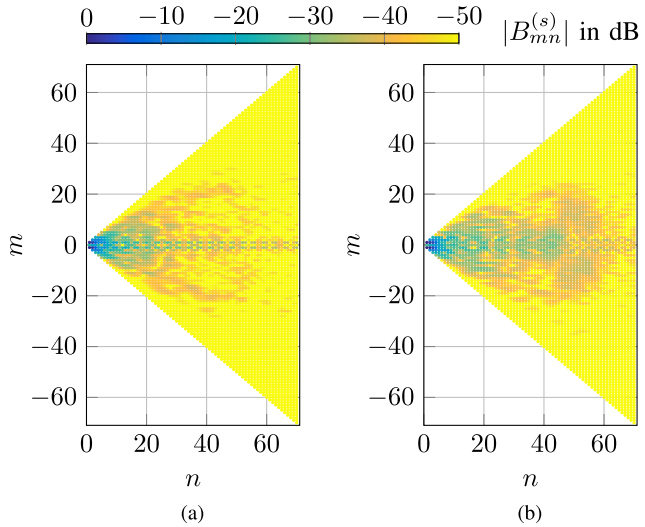

Fig. 10. Mode spectrum of an integrated antenna at 160 GHz in the phase center ($\Delta z = 6$ mm). (a) $B_{mn}^{(1)}$. (b) $B_{mn}^{(2)}$.

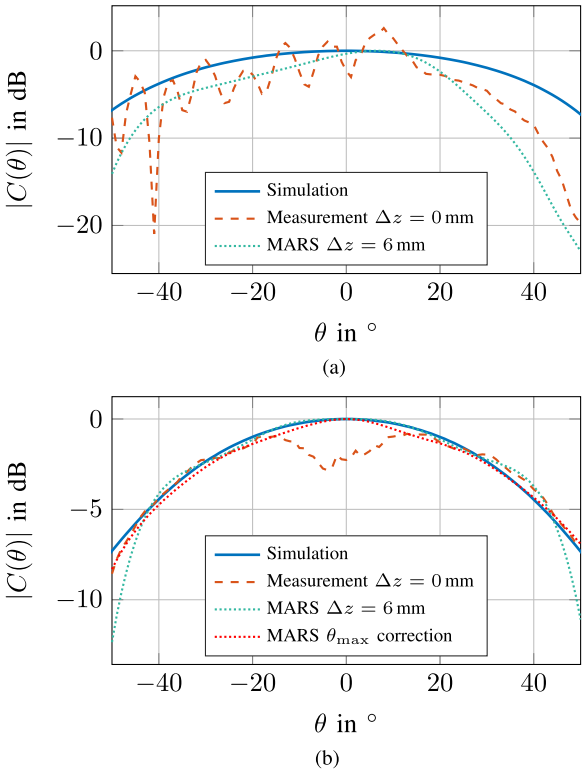

Fig. 11. Comparison of measurement, simulation, and postprocessed radiation pattern of the integrated antenna at 160 GHz for an offset of $\Delta z = 6$ mm. Probe reflections cause strong ripples in the measurements. MARS yielded similar results for $\Delta z = 2$ mm and $\Delta z = 4$ mm. (a) E-plane ($\phi = 0°$). (b) H-plane ($\phi = 90°$).

between the simulation result, a reference far-field measurement with an offset of $\Delta z = 0$, and the results of the MARS algorithm for an offsets $\Delta z = 6$ mm in the E- and H-plane. The antenna was simulated on an infinite ground plane without a wafer probe in order to have an undistorted reference. In the measurement result, the impact of probe reflections can be seen clearly in both planes. Especially, the E-plane (x-z-plane in Fig. 1) is severely distorted and exhibits large ripples due to the superposition of direct and reflected radiation on the

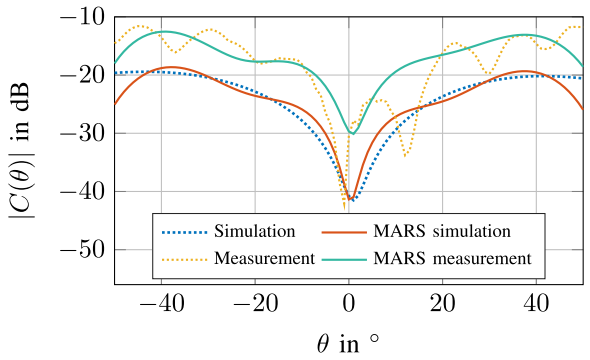

Fig. 12. Comparison between measurement, simulation, and postprocessed cross-polarization in the H-plane at 160 GHz. Distortions were reduced with MARS. The remaining offset is caused by a nonideal resonator position on the chip.

measurement plane. The decline for $\theta > 15°$ is caused by blockage of the signal in the shadow region behind the probe.

The reflections have a smaller effect on the plane orthogonal to the probe plane (y-z-plane Fig. 1). Only the area for $|\theta| < 15°$ is affected by the reflections, showing the same minimum as in the E-plane for $\theta = 0$, due to destructive interference between the direct and reflected signal.

The distortions can be reduced significantly through MARS. The calculated E-plane pattern in Fig. 11(a) does not show any ripples anymore and is much closer to the simulation result. Only the shadowing behind the probe cannot be corrected by MARS. The results that were obtained for different offsets ($\Delta z = 2$ mm and $\Delta z = 4$ mm) were almost identical. The result in the H-plane shows hardly any difference compared with the simulation results, except for the deviation for large θ values, which is, as discussed in Section IV, due to the limited scanning surface. Using the calculated error for $\theta_{\max} = 50°$ and $n_1 = 10$ shown in Fig. 7(b), the error can be subtracted from the postprocessed far-field result, which reduces the error at angles $|\theta| > 50°$ significantly as shown in Fig. 11(b). This, however, is only a valid approach if the simulated and calculated radiation patterns are similar and thus can only be performed in the H-plane for the discussed measurement.

As the back transformation yields the complex E_ϕ and E_θ component, the technique can also be used for circular polarized antennas and cross-polarization analyses. Fig. 12 shows a comparison of the measured and simulated cross-polarization of the integrated antenna at 160 GHz. While the unprocessed measurement is severely distorted, the postprocessed measurement shows a similar progression as the simulation result. The difference between simulation and measurement of approximately 7 dB is caused by a nonideal position of the dielectric resonator, which was manually glued on the chip and is used to improve the radiation efficiency [15]. As the cross-polarization is very sensitive toward the resonator position, even small offsets of around 50 μm can have a significant effect on the cross-polarization level. As already discussed for the copolarization results, the limited scanning surface results in a decrease of the results for large $|\theta|$-values.

The 3-D radiation patterns shown in Fig. 13 also demonstrate how much the measured radiation pattern can be

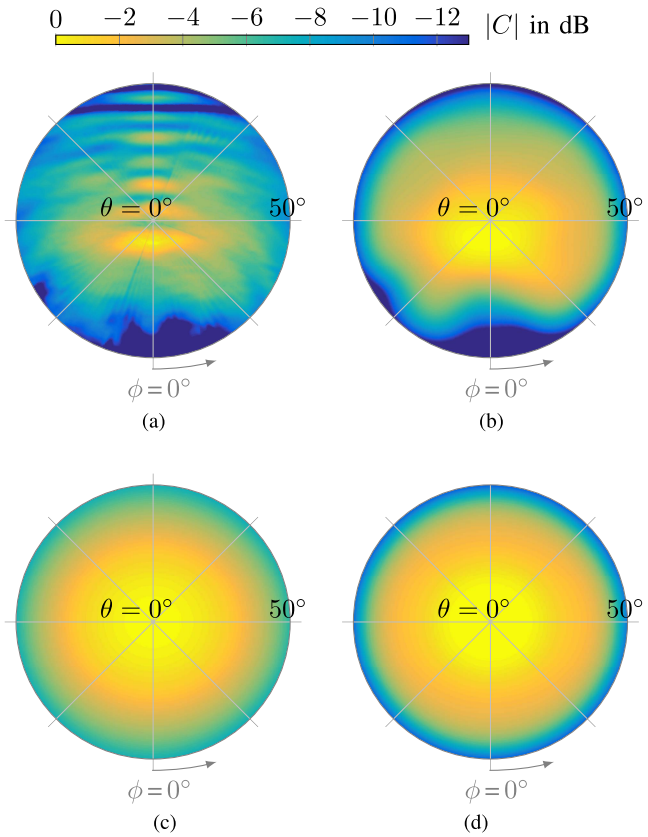

Fig. 13. 3-D radiation pattern of the integrated antenna at 160 GHz. The probe (probe A) is located in $\phi = 0°$-direction. (a) Measurement. (b) MARS result. (c) Simulation. (d) Simulation SWE.

improved through the MARS algorithm. Fig. 13(a) and (c) shows the unprocessed measured/simulated absolute value of the normalized radiation pattern for the integrated antenna at 160 GHz, while Fig. 13(b) and (d) shows the results of the MARS (offset $\Delta z = 6$ mm) algorithm for the measurement and of the SWE ($\Delta z = 0$) result for the simulation. In both cases $\theta_{\max}$ was set to 50° and N to 13.

While the unprocessed measurement shows no resemblance to the simulation, the postprocessed measurement largely agrees with the expected simulation results. The ripples were filtered out completely and the smooth radiation pattern of the antenna was reconstructed. The biggest difference between measurement and simulation after the postprocessing occurs behind the probe in $\phi = 0°$-direction, where the signal was blocked during the measurement.

B. Directivity

The directivity of an antenna can be determined by integration over the normalized radiation pattern $C(\theta, \phi)$ on a sphere around the AUT

$$D = \frac{4\pi}{\int_{\phi=0}^{2\pi} \int_{\theta=0}^{\pi} C^2(\theta, \phi) \sin\theta d\theta d\phi}. \tag{21}$$

The calculated directivity of the simulated integrated antenna is 9.5 dBi.

If the radiation pattern is only known on a section of the sphere, the integration cannot be performed over the entire

surface. If the unknown part of the sphere is assumed to be zero, the value of the denominator in (21) is underestimated, which results in an upper bound for the directivity. With $\theta_{\max} = 50°$ [Fig. 13(c)], the calculated directivity of the simulated antenna increases to 10.2 dBi. The same value is obtained after the SWE [Fig. 13(d)].

In order to obtain a lower bound for the directivity, it was assumed that the directivity for angles $50° < \theta \leq 90°$ is equal to the directivity on the edge at $\theta = 50°$, in which case the integral is overestimated. This resulted in a lower bound of 8.1 and 9.3 dBi for the simulated directivity without and with SWE, respectively. The SWE increases the directivity, because the beamwidth is decreased for θ angles close to 50°, as shown in Fig. 6, but this effect is counteracted by the overestimation of the integral, which is why the lower bound of the SWE is very close to the real directivity.

The distortions of the measurement result [Fig. 13(a)] do not facilitate a meaningful directivity calculation; however, after postprocessing [Fig. 13(b)], the upper and the lower bound of the measured directivity were 11.5 dBi and 10.7 dBi, respectively. The blockage behind the probe, which is not completely reconstructable, and the limited scanning range with the MARS algorithm increase the measured directivity, but the measured values are still reasonably close to the simulated results.

VII. Conclusion

Strong reflections render measurement results unreliable, when measuring integrated antennas with commercially available wafer probes. In order to reduce interferences, the MARS algorithm was applied to integrated antenna measurements for frequencies over 100 GHz for the first time. The effect of a limited scanning surface was analyzed and the impact of a faulty phase center position was discussed. A new method to determine the phase center position that is more robust toward reflections in the measurement setup was proposed.

While the raw measurement results of the integrated antenna are not a meaningful representation of the radiation pattern and cannot be used to determine the directivity of an antenna, the postprocessed results show a much better agreement with the simulations and make it possible, for the first time, to measure the directivity of an integrated antenna with commercially available wafer probes.

References

[1] G. Burrell and A. R. Jamieson, "Antenna radiation pattern measurement using time-to-frequency transformation (TFT) techniques," *IEEE Trans. Antennas Propag.*, vol. 21, no. 5, pp. 702–704, Sep. 1973.

[2] G. Hindman and A. Newell, "Reflection suppression in large spherical near-field range," in *Proc. AMTA 27th Annu. Meeting Symp.*, Newport, RI, USA, 2005.

[3] G. Hindman and A. C. Newell, "Reflection suppression to improve anechoic chamber performance," in *Proc. AMTA Eur.*, 2006, pp. 297–302.

[4] S. F. Gregson, A. C. Newell, and G. E. Hindman, "Reflection suppression in cylindrical near-field measurements of electrically small antennas," in *Proc. 31st Annu. Meeting Symp. Antenna Meas. Techn. Assoc. (AMTA)*, Salt Lake City, UT, USA, Nov. 2009, pp. 393–396.

[5] S. F. Gregson, A. C. Newell, and G. E. Hindman, "Reflection suppression in cylindrical near-field measurements of electrically small antennas," in *Proc. Loughborough Antennas Propag. Conf.*, Nov. 2009, pp. 393–396.

[6] S. F. Gregson, A. C. Newell, G. E. Hindman, and M. J. Carey, "Advances in cylindrical mathematical absorber reflection suppression," in *Proc. 4th Eur. Conf. Antennas Propag.*, Apr. 2010, pp. 1–5.

[7] S. F. Gregson, A. C. Newell, G. E. Hindman, and M. J. Carey, "Application Of Mathematical Absorber Reflection suppression to planar near-field antenna measurements," in *Proc. 5th Eur. Conf. Antennas Propag. (EUCAP)*, Apr. 2011, pp. 3412–3416.

[8] C. Parini, S. Gregson, J. McCormick, and D. J. van Rensburg, *Theory and Practice of Modern Antenna Range Measurements* (IET Electromagnetic Wave Series). London, U.K.: Inst. Eng. Technol., 2014.

[9] S. F. Gregson, J. Dupuy, C. G. Parini, A. C. Newell, and G. E. Hindman, "Application of mathematical absorber reflection suppression to far-field antenna measurements," in *Proc. Loughborough Antennas Propag. Conf.*, Nov. 2011, pp. 1–4.

[10] E. C. Lee, E. Szpindor, and W. E. McKinzie, III, "Mitigating effects of interference in on-chip antenna measurements," in *Proc. AMTA 37th Annu. Meeting Symp.*, Long Beach, CA, USA, Oct. 2015.

[11] W. E. McKinzie, D. M. Nair, B. A. Thrasher, M. A. Smith, E. D. Hughes, and J. M. Parisi, "60 GHz patch antenna in LTCC with an integrated EBG structure for antenna pattern improvements," in *Proc. IEEE Antennas Propag. Soc. Int. Symp. (APSURSI)*, Jul. 2014, pp. 1766–1767.

[12] L. Boehm, F. Boegelsack, M. Hitzler, S. Wiehler, and C. Waldschmidt, "Accuracy evaluation for antenna measurements at mm-wave frequencies," in *Proc. 10th Eur. Conf. Antennas Propag. (EuCAP)*, Apr. 2016, pp. 4009–4013.

[13] L. Boehm, M. Hitzler, F. Roos, and C. Waldschmidt, "Probe influence on integrated antenna measurements at frequencies above 100 GHz," in *Proc. Eur. Microw. Conf. (EuMC)*, London, U.K., Oct. 2016, pp. 552–555.

[14] A. C. F. Reniers, A. R. van Dommele, A. B. Smolders, and M. H. A. J. Herben, "The influence of the probe connection on mm-wave antenna measurements," *IEEE Trans. Antennas Propag.*, vol. 63, no. 9, pp. 3819–3825, Sep. 2015.

[15] D. Hou *et al.*, "D-band on-chip higher-order-mode dielectric-resonator antennas fed by half-mode cavity in CMOS technology," *IEEE Antennas Propag. Mag.*, vol. 56, no. 3, pp. 80–89, Jun. 2014.

[16] P. Morse and H. Feshbach, *Methods of Theoretical Physics Part II*. New York, NY, USA: McGraw-Hill, 1953.

[17] J. A. Stratton, *Electromagnetic Theory*. New York, NY, USA: McGraw-Hill, 1941.

[18] J. E. Hansen, *Spherical Near-Field Antenna Measurements* (IET Electromagnetic Wave Series). London, U.K.: Inst. Eng. Technol., 2008.

[19] A. C. Newell and G. Hindman, "The alignment of a spherical near-field measurement system using electrical measurements," in *Proc. IEEE Antennas Propag. Soc. Int. Symp.*, vol. 3. Jun. 1998, pp. 1327–1330.

[20] A. P. Mynster, J. M. Nielsen, and S. Pivnenko, "Electrical alignment of antenna coordinate system in a planar near-field setup," in *Proc. 5th Eur. Conf. Antennas Propag. (EUCAP)*, Apr. 2011, pp. 678–682.

[21] J. A. Nelder and R. Mead, "A simplex method for function minimization," *Comput. J.*, vol. 7, no. 4, pp. 308–313, 1965.

[22] E. I. Muehldorf, "The phase center of horn antennas," *IEEE Trans. Antennas Propag.*, vol. 18, no. 6, pp. 753–760, Nov. 1970.

[23] L. Boehm, S. Pledl, F. Boegelsack, M. Hitzler, and C. Waldschmidt, "Robotically controlled directivity and gain measurements of integrated antennas at 280 GHz," in *Proc. Eur. Microw. Conf. (EuMC)*, Paris, France, Sep. 2015, pp. 315–318.

[24] L. Boehm and C. Waldschmidt, "Scattering center determination for integrated antenna measurements at mm-wave frequencies," in *Proc. 11th Eur. Conf. Antennas Propag. (EuCAP)*, Mar. 2017, pp. 1622–1625.

Linus Boehm (S'15) received the B.S. degree from the Karlsruhe Institute of Technology, Karlsruhe, Germany, in 2011, and the M.S. degree from Columbia University, New York City, NY, USA, in 2013. He is currently pursuing the Ph.D. degree with the Department of Microwave Engineering, Ulm University, Ulm, Germany.

His current research interests include integrated antenna measurements above 100 GHz to quantify and improve the achievable accuracy and to minimize measurement errors.

Mr. Boehm received the Best Measurement Paper Award at European Conference on Antennas and Propagation in 2016. He serves as a Reviewer for different IEEE TRANSACTIONS.

Alexander Foerstner received the bachelor's degree from the Ulm University of Applied Sciences, Ulm, Germany, in 2014, and the M.S. degree from Ulm University, Ulm, in 2016.

He is currently involved in electromagnetic compatibility of radar and communication devices.

Martin Hitzler (S'13) received the Dipl.Ing. degree in electrical engineering from Ulm University, Ulm, Germany, in 2012, where he is currently pursuing the Ph.D. degree with the Institute of Microwave Engineering.

His current research interests include frequency modulated continuous wave radar sensors, integrated antennas, monolithic microwave integrated circuit packaging, and interconnects, all at millimeter-wave frequencies.

Mr. Hitzler was a recipient of the ARGUS Science Award in 2013.

Christian Waldschmidt (S'01–M'05–SM'13) received the Dipl.Ing. (M.S.E.E.) and Dr.-Ing. (Ph.D.E.E.) degrees from the Karlsruhe Institute of Technology, Karlsruhe, Germany, in 2001 and 2004, respectively.

From 2001 to 2004, he was a Research Assistant with the Institut für Hochfrequenztechnik und Elektronik, Karlsruhe Institute of Technology. Since 2004, he has been with Robert Bosch GmbH, Stuttgart, Germany, in the business units Corporate Research and Chassis Systems. He was heading different research and development teams in microwave engineering, RF-sensing, and automotive radar. In 2013, he returned to academia. He was appointed as the Director of the Institute of Microwave Engineering, Ulm University, Ulm, Germany, as a Full Professor. He has authored or co-authored over 100 scientific publications and over 20 patents. His current research interests include radar and RF-sensing, millimeter-wave and submillimeter-wave engineering, antennas and antenna arrays, and RF and array signal processing.

Dr. Waldschmidt served as the TPC Chair of the IEEE Microwave Theory and Techniques Society International Conference on Microwaves for Intelligent Mobility in 2015. He is the Vice Chair of the IEEE MTT-27 Technical Committee (wireless enabled automotive and vehicular applications), an Executive Committee Board Member of the German Microwave Theory and Techniques/Antennas and Propagation Joint Chapter, and a member of the Information Technology Society committee Microwave Engineering (VDE). He is a Reviewer for multiple IEEE TRANSACTIONS AND LETTERS.